AIP | Review of Scientific Instruments

Battery-powered pulsed high density inductively coupled plasma source for pre-ionization in laboratory astrophysics experiments

Vernon H. Chaplin and Paul M. Bellan

Citation: Review of Scientific Instruments **86**, 073506 (2015); doi: 10.1063/1.4926544
View online: http://dx.doi.org/10.1063/1.4926544
View Table of Contents: http://scitation.aip.org/content/aip/journal/rsi/86/7?ver=pdfcov
Published by the AIP Publishing

Battery-powered pulsed high density inductively coupled plasma source for pre-ionization in laboratory astrophysics experiments

Vernon H. Chaplin[a] and Paul M. Bellan
California Institute of Technology, Pasadena, California 91125, USA

(Received 24 February 2015; accepted 29 June 2015; published online 15 July 2015)

An electrically floating radiofrequency (RF) pre-ionization plasma source has been developed to enable neutral gas breakdown at lower pressures and to access new experimental regimes in the Caltech laboratory astrophysics experiments. The source uses a customized 13.56 MHz class D RF power amplifier that is powered by AA batteries, allowing it to safely float at 3–6 kV with the electrodes of the high voltage pulsed power experiments. The amplifier, which is capable of 3 kW output power in pulsed (<1 ms) operation, couples electrical energy to the plasma through an antenna external to the 1.1 cm radius discharge tube. By comparing the predictions of a global equilibrium discharge model with the measured scalings of plasma density with RF power input and axial magnetic field strength, we demonstrate that inductive coupling (rather than capacitive coupling or wave damping) is the dominant energy transfer mechanism. Peak ion densities exceeding 5×10^{19} m^{-3} in argon gas at 30 mTorr have been achieved with and without a background field. Installation of the pre-ionization source on a magnetohydrodynamically driven jet experiment reduced the breakdown time and jitter and allowed for the creation of hotter, faster argon plasma jets than was previously possible. © *2015 AIP Publishing LLC.* [http://dx.doi.org/10.1063/1.4926544]

I. INTRODUCTION

The Caltech magnetohydrodynamically driven jet and current-carrying flux tube experiments[1,2] use pulsed power technology[3] to initiate high density (10^{20}–10^{23} m^{-3}) arc discharges by breaking down a neutral gas cloud. Because the plasmas approximately satisfy the criteria for ideal magnetohydrodynamics (MHD), which is a scale-invariant theory, the experiments may be relevant to astrophysical phenomena ranging from solar coronal loops and coronal mass ejections[4] to astrophysical jets associated with protostars and active galactic nuclei,[5] provided that an electrode geometry appropriate for each case is selected. Previous experimental results have yielded fundamental insights into the physics of spheromak formation,[6,7] demonstrated the importance of non-equilibrium, MHD-driven flows in the expansion and collimation of current-carrying flux tubes,[2] and identified a mechanism by which MHD plasmas may undergo fast magnetic reconnection as a result of a multiscale instability cascade.[8]

The MHD-driven jet experiment sequence is described in the caption of Fig. 1. In the absence of pre-ionization, the Paschen criterion for neutral gas breakdown in a DC electric field sets a lower limit on the neutral gas pressure necessary to initiate the experiment, restricting the parameter space that can be accessed. However, if plasma is already present when a voltage is applied across the electrodes, then the Paschen criterion does not apply, and full plasma breakdown may be achieved with a lower neutral gas density. We have developed a radiofrequency (RF) pre-ionization source to produce this seed plasma, allowing for the creation of lower mass jets that are hotter and faster than those in previous experiments.

Low pressure RF plasmas, which include capacitively coupled plasmas (CCPs), inductively coupled plasmas (ICPs), and wave-heated plasmas (WHPs) such as helicons, are widely used in industrial materials processing,[9] as well as in other fields such as electric propulsion[10] and bioengineering.[11] They have been used for pre-ionization in at least one spheromak experiment similar to the Caltech experiments[12] and also to assist startup in some tokamaks.[13] In our experiment, 2-3 kW of RF power was delivered to the plasma through an external antenna by a customized pulsed 13.56 MHz RF amplifier. The amplifier was powered by AA batteries, which charged up a capacitor to store ~2 J of energy for each 0.1–1 ms RF pulse. This design enabled the entire pre-ionization source to float electrically, a critical safety feature since it would be installed in the vicinity of conductors that would charge up to 3–6 kV when the main capacitor bank of the pulsed power experiment was fired. Pulsed operation meant that the RF amplifier could be very compact, since no cooling apparatus was necessary.

II. DETAILS OF PLASMA SOURCE DESIGN

A block diagram of the pre-ionization plasma source and the RF amplifier is shown in Fig. 2. The RF plasma was created in a 33.0 cm long, 2.54 cm outer diameter (OD), and ~2.2 cm inner diameter (ID) quartz tube, which was surrounded by the RF antenna and by a solenoid powered by an electrically floating capacitor discharge circuit. The dimensions of the discharge tube and solenoid were chosen so that they could be installed behind the central electrode of the MHD-driven jet experiment with minimal modifications to the original experiment's plasma gun design. Several antenna geometries were tested. A 10.5 cm long half-turn helical antenna,[14] wound tightly onto the quartz tube using thin copper strips, produced the highest plasma densities and

[a]Electronic mail: vernon.chaplin@gmail.com

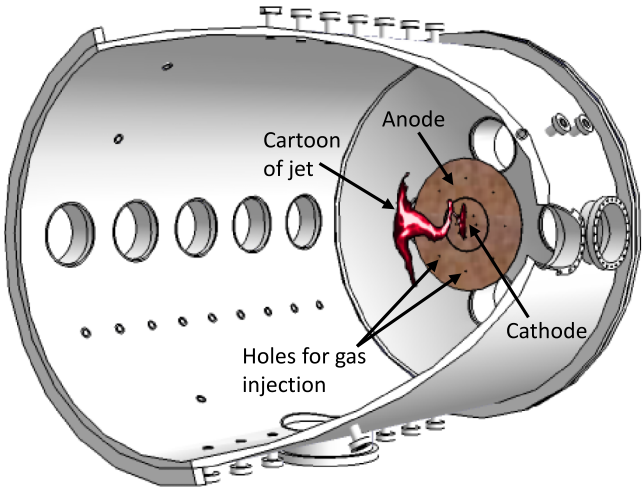

FIG. 1. The Caltech MHD-driven jet experiment. The electrodes, consisting of a circular cathode surrounded by an annular anode, are mounted on one end dome of a cylindrical vacuum chamber. A coil behind the cathode (labeled "bias field coil" in Fig. 3) creates an arched, dipole-like magnetic field linking the electrodes, analogous to a protostellar field linking an accretion disk. In experiments without pre-ionization, gas is injected through 8 holes in each of the inner and outer electrodes, and 3–6 kV is applied between the electrodes by an ignitron-switched capacitor bank, breaking down the gas and driving a current in the poloidal (axial and radial) direction. The resulting toroidal (azimuthal) magnetic field pressure gradient drives a jet along the machine axis.

was used for all of the experiments described here. This type of antenna has previously been used to excite helicon plasmas,[14,15] an extremely efficient class of RF discharges that take advantage of wave damping and possibly mode conversion[16,17] to produce high density ($>10^{19}$ m^{-3}) plasmas with relatively low input power (~1 kW). Helicon mode operation was expected in our experiment, but it was not conclusively observed; instead, the discharge was found to be primarily inductively coupled. See Sec. V B for detailed discussion.

Plasma created inside the antenna diffused down the tube and entered the main vacuum chamber as shown schematically in Fig. 3, with radial confinement provided by the applied axial magnetic field. The main chamber had radius 45.7 cm and length 114.3 cm and was pumped to a base pressure of $\sim 5 \times 10^{-7}$ Torr by a Leybold Turbovac 1000 turbo pump, which was mounted on top of the chamber and was backed by an Edwards XDS10 scroll pump. For pre-ionized MHD-driven jet experiments, gas was delivered to the discharge tube through a feedthrough at the rear end of the tube by a fast pulsed gas valve.[18] During testing and optimization of the pre-ionization source, a variable leak valve (Granville-Phillips Series 203) attached to a feedthrough near the center of the main chamber was used to produce a uniform fill pressure. An ultraviolet (UV) flashlamp (Excelitas Technologies model FX-1165 Metal Can Xenon Flashlamp with Reflector) was attached to the end of the discharge tube behind the gas feed connection—firing this lamp at the time of RF turn-on provided seed ionization that improved the consistency of the RF plasma breakdown and made the time-dependent behavior of the experiment extremely reproducible.

III. RF POWER AMPLIFIER

A. Amplifier circuit

The central component of the 13.56 MHz RF amplifier, shown in the photo in Fig. 4(a), was the Microsemi DRF1301 power MOSFET hybrid,[19] a compact 1 in. × 2 in. module containing two power MOSFETs (rated for BV_{DSS} = 1000 V and I_D = 15 A and capable of 30 MHz switching) along with

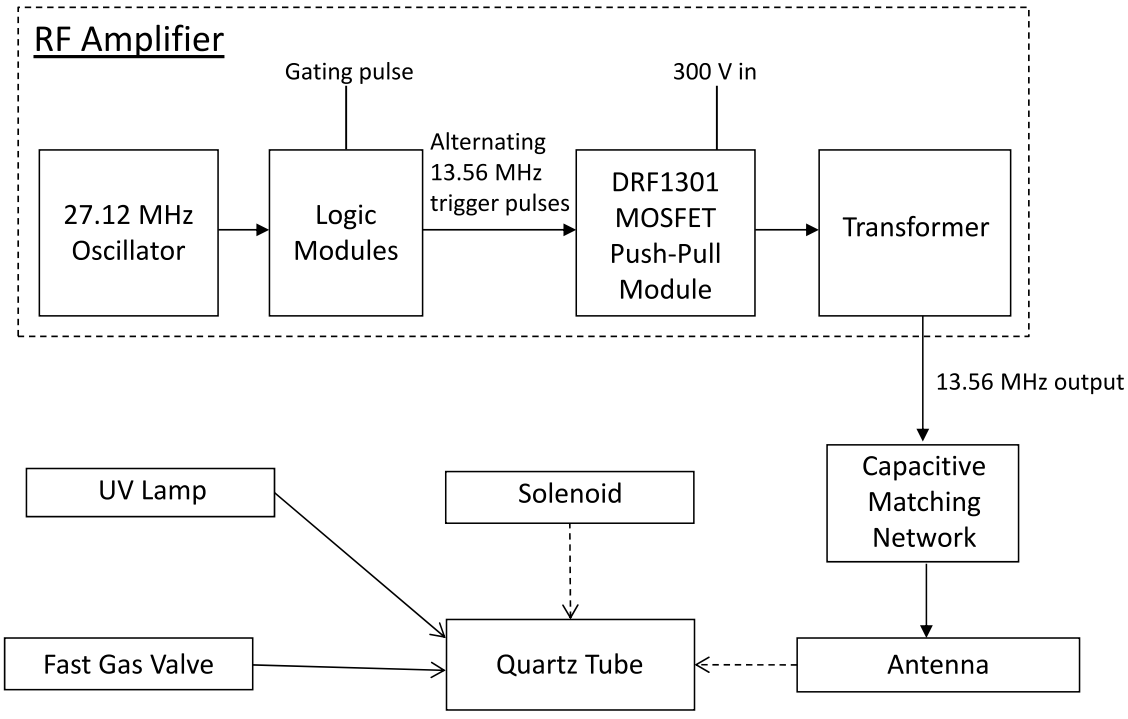

FIG. 2. Block diagram for the pre-ionization plasma source, showing the main sections of the RF amplifier and the other key components described in the text.

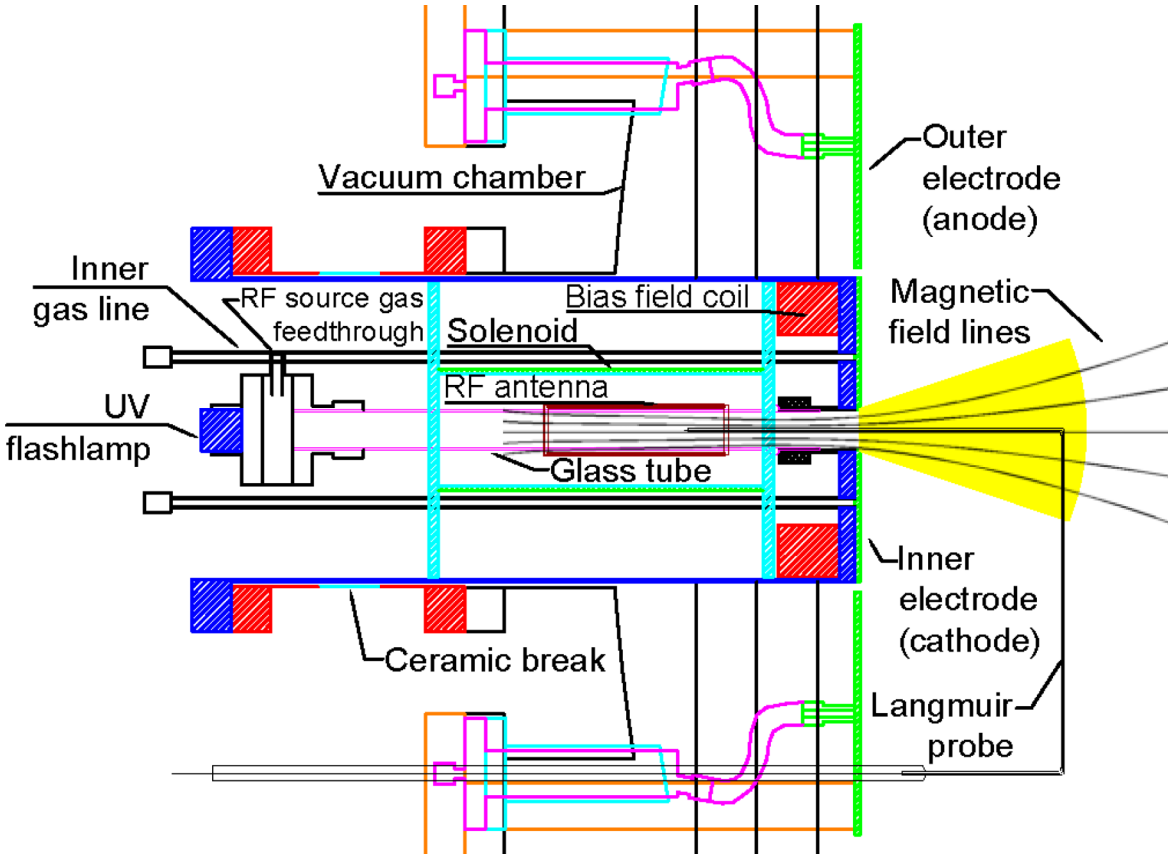

FIG. 3. 2D computer aided design (CAD) drawing showing the source installed on the MHD-driven jet experiment. The jet experiment's electrodes appear as thin rectangles at the right-hand side of the figure in this side-on, cross-sectional view. The anode was attached to the grounded vacuum chamber, while the cathode and all attached components, including the pre-ionization source, charged up to (−3)–(−6) kV when the main capacitor bank was triggered. The RF plasma expanded into the chamber along the background magnetic field through a hole in the center of the cathode, as illustrated in the figure.

high power gate drivers. The amplifier design, which may be categorized as a transformer-coupled voltage-switching (TCVS) class D configuration, was based on a circuit described in a Microsemi application note by Choi,[20] which was modified here for pulsed operation. A schematic of the output stage is shown in Fig. 5. When the MOSFET $Q1$ is switched on and $Q2$ is switched off, current flows from the 47 μF capacitor $C1$ (charged by the AA batteries through an EMCO Q03-12 proportional DC power supply to $V_{ps} \leq 300$ V) through the upper half of the center-tapped primary winding of the transformer and through $Q1$ to ground. The voltage drop across $Q1$ is small when it is switched on, so assuming that the transformer behaves ideally, there is a voltage V_{ps} across each half of the primary. Thus, the voltage at the drain of $Q2$ is $2V_{ps}$, and the output voltage across the transformer secondary is $(n/m)\,V_{ps}$. Over the next half-cycle, $Q2$ turns on, $Q1$ turns off, and the polarity of the output voltage reverses.

Trigger pulses to turn on the MOSFETs are provided by the low-voltage pulse generation circuit shown in Fig. 6. The 27.12 MHz oscillator $U2$ runs continuously when the amplifier's batteries are connected. The RF output is enabled by an optical gating signal received by $U1$, which turns off the NPN transistor $Q1$ and causes the pin $2D$ of the IC $U3$ to go to a high logic level. The left side of $U3$ (pins 1–7) is used to split the 27.12 MHz signal from the oscillator into two 13.56 MHz pulse trains (output at pins $1Q$ and $1\overline{Q}$) that are 180° out of phase. The logic may be understood by inspecting the truth table for $U3$ (Table I).

Before being sent to the MOSFET gates, the outputs from pins $1Q$ and $1\overline{Q}$ of $U3$ are passed through additional logic circuits that allow the user to adjust the pulse widths (duty cycle) and relative phase of the two pulse trains. Driving each MOSFET at somewhat less than 50% duty cycle is generally necessary for stable operation. The circuit for the $1Q$ output, which consists of the right side of $U3$ (pins 8–14) and the attached components, is included in the diagram in Fig. 6. Since $2D$ is held high, the output $2Q$ goes high on the rising edge of the signal received from $1Q$ at $2CLK$, turning on MOSFET #1. $2Q$ goes low again when a low level is received at $2\overline{CLR}$, which occurs after an interval that can be adjusted by varying $R11$. Meanwhile, $R7$ controls the overall phase delay of the trigger pulses for MOSFET #1.

The output from pin $1\overline{Q}$ of $U3$ goes to a second logic circuit (not shown in Fig. 6) that produces a 13.56 MHz pulse train with an adjustable duty cycle for controlling MOSFET #2. This portion of the circuit uses another SN74ACT74 flip-flop and is identical to the circuit attached to the right side of $U3$, except that the phase adjustment potentiometer $R7$ is replaced by a fixed 220 Ω resistor.

Due to the compact size of the circuit board, it was critical to use surface mount rather than through-hole components for the low-voltage circuitry to avoid excessive feedback from the high voltage output stage. Another key practical consideration

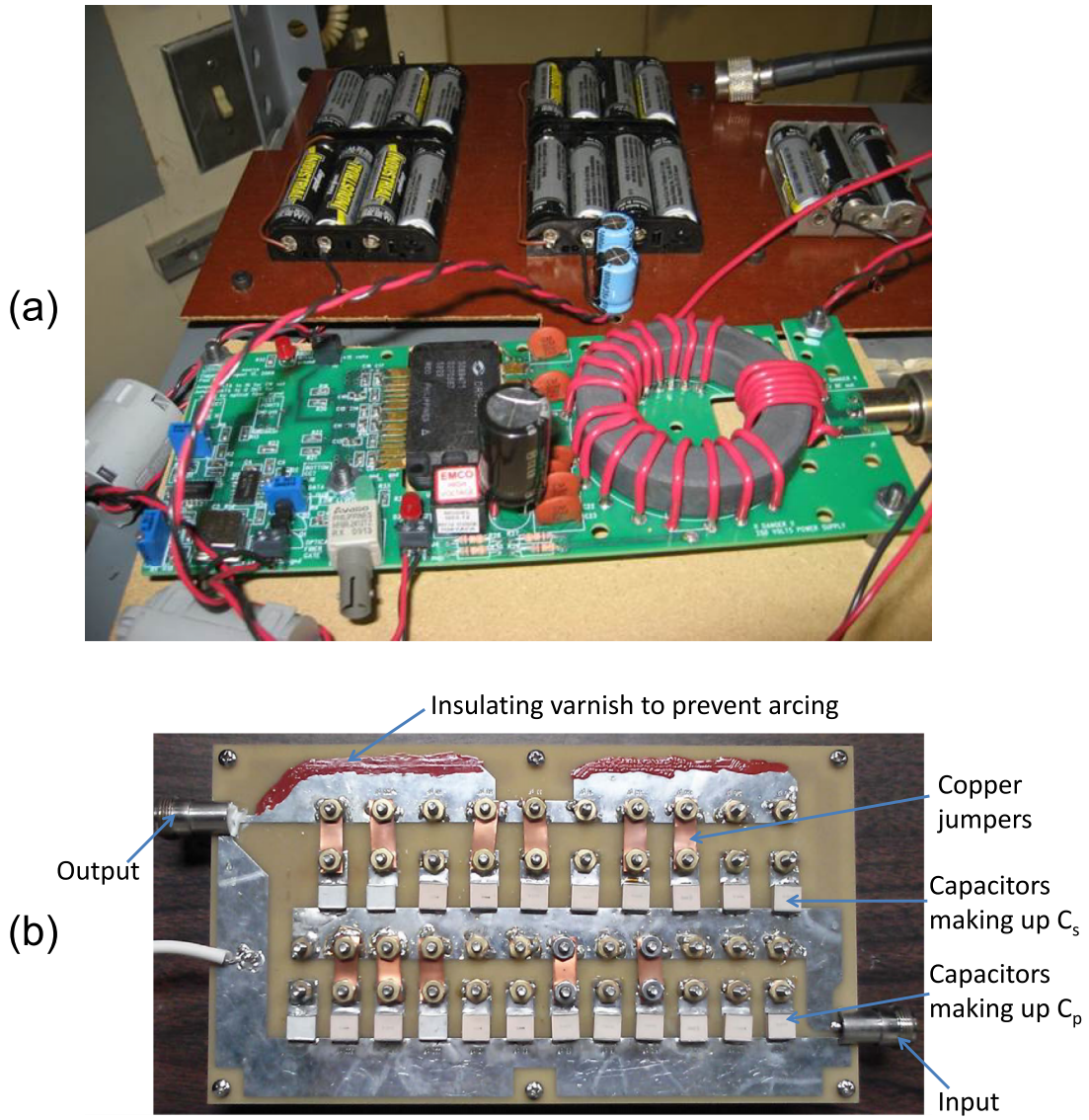

FIG. 4. (a) Photo of the 3 kW RF power amplifier, which was mounted on a 3 in. × 7.5 in. printed circuit board, and the AA batteries that powered it. (b) Photo of the binary arrays of impedance matching capacitors. Individual capacitors could be disconnected from the circuit by removing the corresponding copper jumper.

was the construction of the high-frequency center-tapped transformer, which was wound with 16 American wire gauge (AWG) wire on an Amidon FT240-61 ferrite toroid. Each half of the primary had a single turn composed of 8 windings in parallel in order to reduce resistive losses in the windings. The number of secondary turns was adjustable from 1 to 6, and multiple windings in parallel were again used when space permitted.

The amplifier required a total of 3 AA batteries for the pulse generation stage, 8–9 AA batteries for the driver stage (which consisted simply of a voltage supplied directly to the DRF1301 driver power supply inputs through 0.25 Ω resistors), and 1–8 AA batteries for the output stage, depending on the desired value of V_{ps}. The DRF1301s tended to develop a fault in which they would draw excessive steady-state current into the driver stage, so the driver stage batteries were used to charge up a 2 mF capacitance through a 150 Ω resistor in order to keep the batteries from being drained too fast in between RF amplifier pulses. The quiescent current drawn by the driver stage through this limiting resistor was ~25 mA, so assuming the useful output capacity of each battery was 500 mAh = 1800 C (alkaline batteries rated for 2750 mAh were typically used, but the output voltage was too low to power the driver over much of the rated battery lifetime), the amplifier could be left on for ~20 h before the driver batteries needed to be replaced. This estimate agrees well with the observed performance. The lifetime of the final stage batteries was similar; in typical operation with the amplifier pulsed roughly once per minute, the dominant energy sink was the ~0.2 W continuously dissipated in the 500 kΩ safety bleeder resistor installed across the 47 μF output stage capacitor, rather than the 1–2 J stored energy needed for each RF pulse. In portable applications for which battery lifetime is an important concern, this bleeder resistor could be disconnected from the circuit using relays that open when the amplifier is turned on, enabling the amplifier to be pulsed several thousand times without replacing or recharging the final stage batteries.

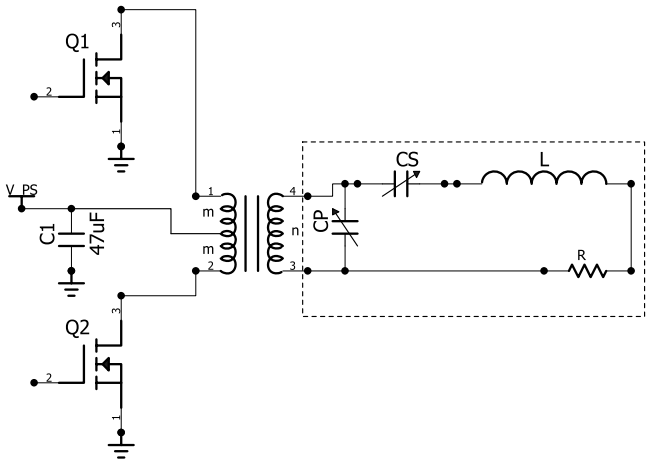

FIG. 5. Schematic of the RF amplifier output stage. $Q1$ and $Q2$ are the power MOSFETs located inside the DRF1301. The dashed box surrounds the load, consisting of the antenna, plasma, and impedance matching capacitors. The antenna was connected to the matching capacitors by a ~40 cm length of 50 Ω coaxial cable; since its length was short compared to the signal wavelength at 13.56 MHz ($\lambda \sim 15$ m), the cable acted as a lumped impedance that added to the series inductance of the antenna. The compactness of the amplifier allowed it to be installed in close proximity to the location where the RF power was needed, avoiding the use of a long transmission line, which would have required that both the source and the load be separately matched to the characteristic cable impedance in order to avoid reflected power.

When the pre-ionization source was installed on the MHD-driven jet experiment, the ground reference of the RF amplifier was attached to the high voltage cathode of the jet experiment through a 15 Ω high pulse energy non-inductive resistor (Carborundum Co. 887AS series), so that the entire pre-ionization system would follow changes in the cathode voltage. The floating capacitor banks powering the bias field coil, the solenoid, and the fast gas valves for the pre-ionization source and cathode gas inlets were also connected to the cathode through this resistor.

TABLE I. Partial truth table for the SN74ACT74 flip flop, valid when the $P\bar{R}E$ input is held high. "H" stands for a high logic level, "L" for a low level, and ↑ is a rising edge trigger.

Inputs			Outputs	
$\overline{CLR}$	CLK	D	Q	$\overline{Q}$
L	X	X	L	H
H	↑	H	H	L
H	↑	L	L	H

B. Impedance matching and output power

The power output of the RF amplifier was determined by directly measuring the voltage (with a Tektronix P6015 high voltage probe) and current (with an Ion Physics CM-100-M current transformer) at the secondary of the transformer, then multiplying these waveforms together numerically to determine $P_L = \langle I_L V_L \rangle$ averaged over several RF periods (see Fig. 7(b)). The relative phase offset of the voltage and current diagnostics was determined from tests with a resistive load, for which V_L and I_L were known to be approximately in phase (see Fig. 7(a)). The apparent phase difference in the raw data was $\Delta\phi \approx 9$ ns (of which ~6 ns was accounted for by the difference in cable lengths), so this correction was applied in all subsequent power measurements. Throughout this paper, we have calculated error bars on the power by assuming ±1 ns uncertainty in the relative phase. Generally, this led to $< \pm 10\%$ uncertainty in P_L, except in cases in which the voltage and current were nearly 90° out of phase.

When the amplifier was used to drive an antenna and create a plasma, the load impedance was tuned to satisfy the conjugate matching condition $Z_L = Z_S^*$ for maximum power transfer by adjusting the output transformer turns ratio n/m and the variable capacitances C_p and C_s shown in Fig. 5. These were implemented with binary arrays (1 pF, 2 pF, 4 pF,

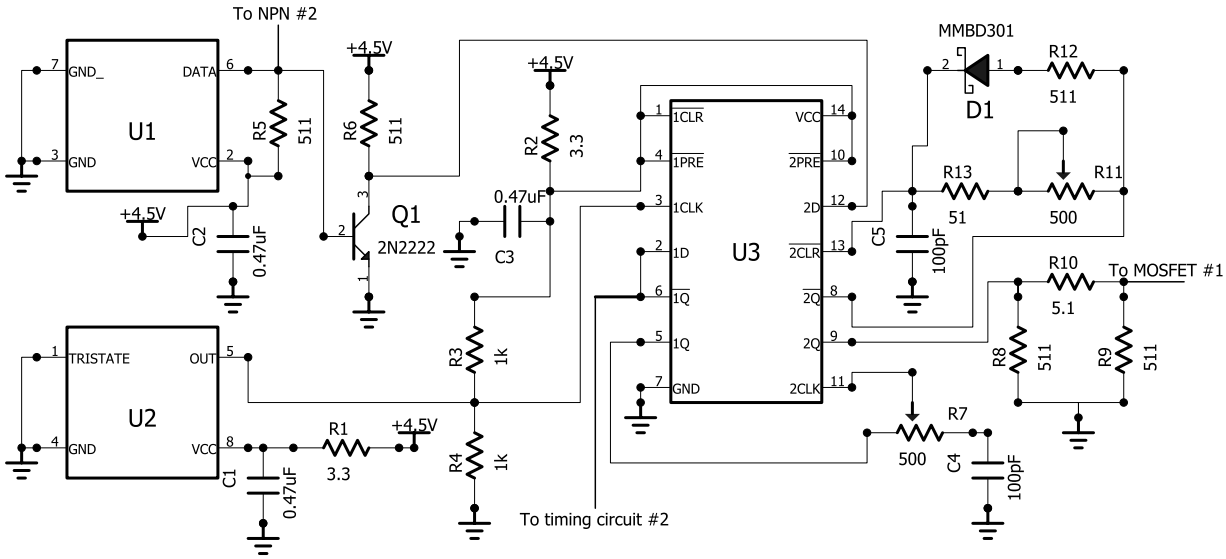

FIG. 6. Partial circuit diagram for the RF amplifier's pulse generation stage. $U1$ is a fiber optic receiver (Avago Technologies HFBR-2412), $U2$ is a 27.12 MHz crystal oscillator (Ecliptek EP1100HSTSC-27.120MHZ), and $U3$ is a dual flip-flop logic IC (Texas Instruments SN74ACT74). The logic circuitry was designed by Choi[20] and is shown here for the convenience of the reader—the new addition in our RF amplifier is the optical gating circuit, consisting of $U1$ and the switching transistor $Q1$ along with the attached resistors and capacitor.

etc.) of high-voltage, low-dissipation fixed value capacitors (American Technical Ceramics 100 E Series and AVX HQCE Hi-Q Series) that could be switched into or out of the circuit as necessary to achieve any desired values for C_p and C_s (see the photo in Fig. 4(b)). The series inductor and resistor in Fig. 5 represent the antenna and plasma; we may roughly model the loading of the antenna by the plasma as a radiation resistance $R_{rad.} \equiv P_{RF}/\langle I_{ant.}^2 \rangle$ that adds to the resistance of the antenna, although in reality the antenna reactance will be modified as well if there is any capacitive or inductive coupling between the antenna and plasma.[9]

The radiation resistance depended on the plasma parameters and was not well known, and the source output impedance, which was determined by non-ideal effects such as the finite on-state resistance and output capacitance of the MOSFETs and parasitic inductance in the amplifier circuit, was also unknown and was not restricted to be real. Thus, the impedance matching was carried out empirically by pulsing the source repeatedly and modifying the values of C_s and C_p until the power delivered to the load or the plasma density was maximized. An example is shown in Fig. 8. P_L was always maximized

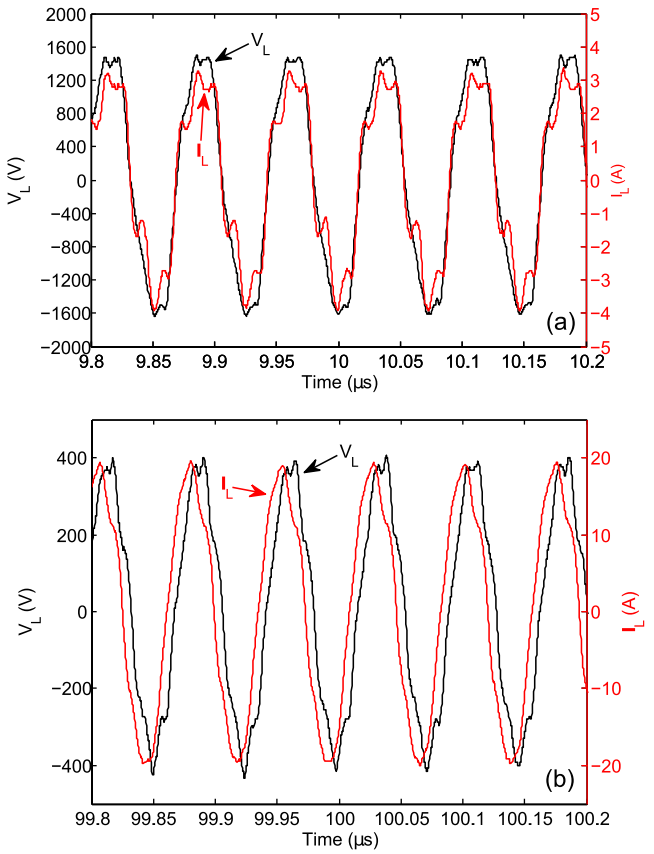

FIG. 7. (a) RF amplifier output voltage and current into a 470 Ω resistive load, with a transformer turns ratio $n/m = 6/1$. The output power for this test was $P_L = \langle I_L V_L \rangle \approx 2.70$ kW. Some ringing is evident in the current monitor waveform, but this effect was less severe in measurements with a plasma load, for which the output waveform was further from a square wave. (b) Amplifier output voltage and current during an argon plasma discharge with $p_{Ar} = 10$ mTorr and $B = 340$ G. The average power transferred was $P_L = \langle I_L V_L \rangle = 3.12^{+0.15}_{-0.17}$ kW, the phase shift between I_L and V_L was $\phi \approx 7$ ns, and the magnitude of the load impedance was $|Z_L| = |V_L|/|I_L| \approx 20\,\Omega$. $n/m = 1/1$ was used in this case; in general, setting $n/m \leq 2$ was necessary to achieve efficient power transfer to the load and high plasma density.

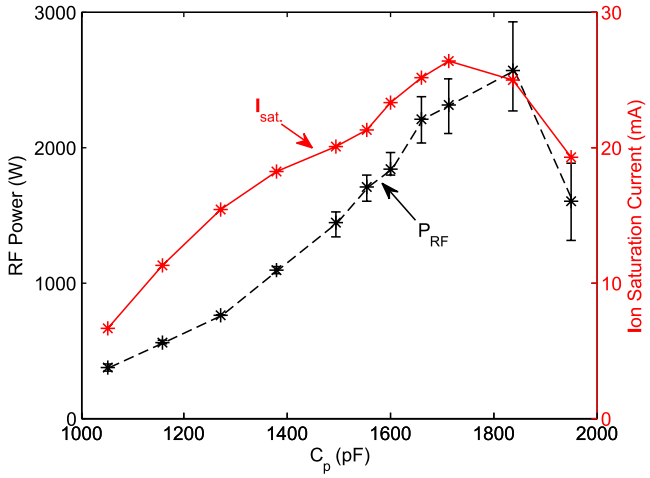

FIG. 8. RF power and Langmuir probe ion saturation current as a function of C_p, with C_s held fixed at 756 pF. The measurements were taken during argon plasma discharges with $p_{Ar} = 30$ mTorr and $B = 340$ G.

with the output current leading the voltage, meaning that the impedance of the load (including the matching capacitors, antenna, and plasma) had a negative imaginary part; i.e., it was capacitive. The conjugate matching condition thus implies that the source output impedance was somewhat inductive.

In addition to choosing values of C_p and C_s that made the magnitude and phase of the load impedance satisfy $Z_L = Z_S^*$, it was important to choose C_s such that the series LC circuit that it formed with the antenna inductance was nearly resonant at 13.56 MHz, in order to have a high RF voltage across the antenna at early times to initiate the discharge. It is believed that all inductively coupled and wave-heated RF discharges must start out in a capacitively coupled mode immediately after plasma breakdown before the density has built up enough to support other modes of operation.[21]

IV. GLOBAL DISCHARGE MODEL

We will interpret our results with the aid of a global steady state model of the RF discharge, in which particle and energy inputs and losses are balanced in order to derive the equilibrium electron temperature (T_e) and density ($n_e = n_i$). The model takes into account multistep ionization by solving for the population densities of neutral argon (Ar I) excited states, which are grouped into three effective energy levels: $4s$ resonant (with statistical weight $g_r = 6$), $4s$ metastable ($g_m = 6$), and $4p$ ($g_p = 36$). Neutral bound states above the $4p$ level and excited ion states are neglected. Similar models for low pressure argon RF discharges have been developed by a number of authors,[22,23] but to our knowledge, no results have been presented for plasma densities greater than 10^{19} m^{-3}.

We assume that the electron velocity distribution is Maxwellian with T_e spatially uniform, and also that the plasma density is approximately uniform over most of the volume of the discharge (consisting of a cylinder of length L and radius R) and then drops rapidly at the sheaths. A flat density profile is a reasonable approximation[9] when the ion-neutral collision mean free path satisfies $\lambda_{in} \gtrsim (T_i/T_e)\,L$. In this regime, the ion flow velocity $|\mathbf{u}_i|$ due to ambipolar

diffusion is greater than the ion thermal velocity v_{Ti}, and as a result, the ion-neutral collision frequency depends on $|\mathbf{u}_i|$, which makes the ambipolar diffusion equation nonlinear. Solution of this nonlinear diffusion equation yields the ratios of the radial and axial sheath edge densities n_{sR} and n_{sL} to the central density n_{e0}, which can be approximated by[9]

$$\frac{n_{sR}}{n_{e0}} \approx 0.80\left(4+\frac{R}{\lambda_{in}}\right)^{-1/2}, \tag{1}$$

$$\frac{n_{sL}}{n_{e0}} \approx 0.86\left(3+\frac{L}{2\lambda_{in}}\right)^{-1/2}. \tag{2}$$

The discharge volume is assumed to be bounded by the antenna length, which is a good approximation in the unmagnetized case. Volume recombination is neglected. Requiring that electron-impact ionization balances radial and axial losses yields

$$\pi R^2 L n_e\left(K_{gi}n_g + K_{mi}n_m + K_{ri}n_r + K_{pi}n_p\right) = c_s\left(2\pi RLn_{sR} + 2\pi R^2 n_{sL}\right), \tag{3}$$

where the $K_{\alpha\beta}$ are temperature-dependent rate coefficients for collisional transitions from state α to state β, with the subscripts defined as illustrated in Fig. 9(a). The Ar I ground state density is calculated as $n_g = n_{total} - (n_e + n_m + n_r + n_p)$, where $n_{total} \propto p_{Ar}$ is the total number of argon atoms in the discharge volume (assumed to be constant) and the density of Ar III ions is assumed to be negligible. Formulas for all rate coefficients used in the model as a function of T_e were taken from the work of Lieberman and Lichtenberg,[9] Table 3.3.

The global power balance equation is

$$P_{RF} = \pi R^2 L n_e\left[K_{gi}n_g E_{gi} + K_{mi}n_m E_{mi} + K_{ri}n_r E_{ri} + K_{pi}n_p E_{pi} + \sum_{\alpha,\beta} K_{\alpha\beta}n_\alpha E_{\alpha\beta} + K_{el.}n_g E_{el.}\right] + c_s\left(2\pi RLn_{sR} + 2\pi R^2 n_{sL}\right)\left[\left(eV_s + \frac{1}{2}k_B T_e\right) + 2k_B T_e\right]. \tag{4}$$

The right hand side includes electron energy losses and gains due to collisional ionization (the first four terms), collisional excitation and de-excitation (represented by the summation over α and β), and elastic scattering with neutrals (with rate coefficient $K_{el.}$ and mean energy transfer[9] $E_{el.} = (3m_e/M_i)\,k_B T_e$), as well as energy carried to the walls by particles lost from the plasma ($[eV_s + \frac{1}{2}k_B T_e]$ per ion and $2k_B T_e$ per electron). The sheath voltage drop is $V_s \approx 4.7 k_B T_e/e$ for argon ICPs and WHPs, but it is much larger for CCPs, approximately 40% of the applied RF voltage amplitude.[9] As a result, for a given RF power level, CCPs cannot produce plasma densities as high as ICPs and WHPs, because too much energy is carried to the walls by ions falling into the deep sheath potential well.

The 4s metastable state population balance (see Fig. 9(a)) is described by

$$K_{gm}n_g n_e + K_{rm}n_r n_e + \left(K_{pm}n_e + A_{pm,eff.}\right)n_p = \left(K_{mr} + K_{mp} + K_{mg} + K_{mi}\right)n_e n_m. \tag{5}$$

The loss rate of metastable atoms by diffusion to the walls[22] is smaller than the collisional de-population rate by at least two orders of magnitude and can be neglected. The analogous balance equations for the 4s resonant and 4p states are

$$K_{gr}n_g n_e + K_{mr}n_m n_e + \left(K_{pr}n_e + A_{pr,eff.}\right)n_p = \left(\left(K_{rm} + K_{rp} + K_{rg} + K_{ri}\right)n_e + A_{rg,eff.}\right)n_r, \tag{6}$$

$$K_{gp}n_g n_e + K_{mp}n_m n_e + K_{rp}n_r n_e = \left(\left(K_{pm} + K_{pr} + K_{pg} + K_{pi}\right)n_e + A_{pm,eff.} + A_{pr,eff.}\right)n_p. \tag{7}$$

The $A_{\alpha\beta,eff.}$ are effective spontaneous transition rates that take into account re-absorption of radiation. We follow Ashida *et al.*[22] and assume that all photons emitted at a distance $d > l_{mfp}$ from the edge of the plasma are re-absorbed, while those emitted within one absorption mean free path l_{mfp} of the boundary escape. The line center absorption cross section (including the effect of stimulated emission) for a Doppler-broadened emission line[24] is

$$\sigma_{\lambda_0} = \frac{\lambda_0^3}{8\sqrt{2}\pi^{3/2}}\frac{g_\alpha}{g_\beta}A_{\alpha\beta}\left(1 - \frac{g_\beta n_\alpha}{g_\alpha n_\beta}\right)\sqrt{\frac{M}{k_B T_g}}, \tag{8}$$

where $M = 6.7\times10^{-26}$ kg for argon and the gas temperature T_g was assumed to be 600 K. The effective transition rates are given by

$$A_{\alpha\beta,eff.} = A_{\alpha\beta}\left(\frac{\pi R^2 L - \pi\left(R - l_{mfp}\right)^2\left(L - 2l_{mfp}\right)}{\pi R^2 L}\right), \tag{9}$$

where $l_{mfp} = \left(n_\beta \sigma_{\lambda_0}\right)^{-1}$. The overall effective transition rates out of the 4s resonant and 4p manifolds are determined by first calculating $A_{\alpha\beta,eff.}$ for each individual spontaneous transition depopulating a 4s resonant or 4p level and then taking a weighted average of these (for example, $A_{pm,eff.} = \sum g_\alpha A_{\alpha\beta,eff.}/36$).

The equilibrium discharge properties were found by numerically solving the system of nonlinear equations (3)–(7) for T_e, n_e, n_m, n_r, and n_p. We started with initial guesses for $A_{rg,eff.}$, $A_{pm,eff.}$, and $A_{pr,eff.}$, then updated these using the excited state population densities predicted by the model, iterating until the calculation converged to a self-consistent solution.

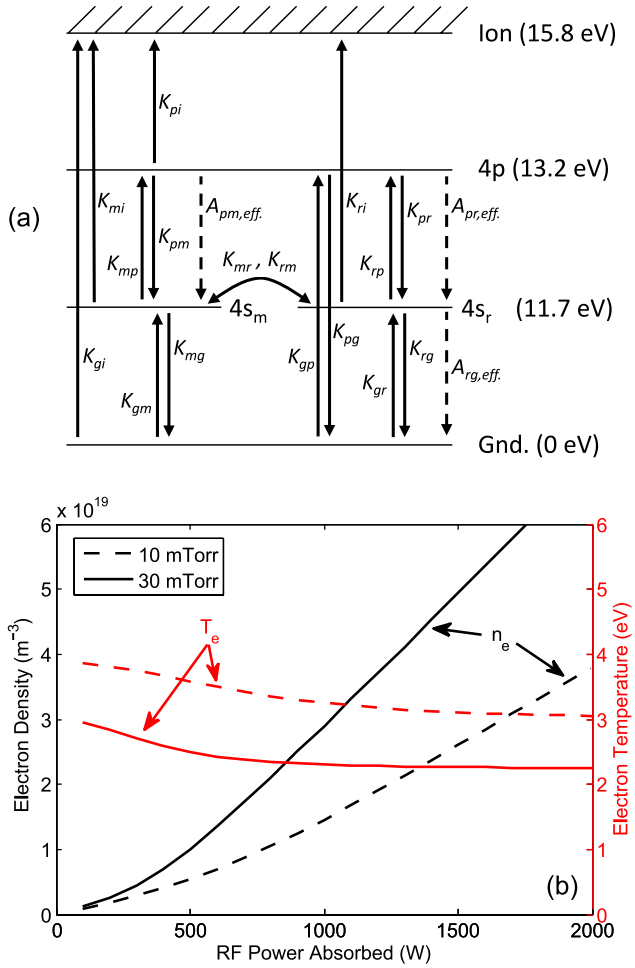

FIG. 9. (a) Ar I energy level structure (not to scale) and collisional and radiative transitions included in the global discharge model. Solid arrows indicate electron-impact excitations and de-excitations with rate coefficients $K_{\alpha\beta}$, and dotted lines indicate spontaneous transitions with absorption-corrected transition rates $A_{\alpha\beta,eff.}$. (b) T_e and n_e vs. RF power calculated by the model for unmagnetized argon ICPs with $L = 10.5$ cm and $R = 1.1$ cm.

The predicted electron temperature and density as a function of RF power for unmagnetized ICPs at 10 mTorr and 30 mTorr are shown in Fig. 9(b). Detailed examination of the model results reveals that stepwise ionization is dominant in the regime of interest: for example, at $p_{Ar} = 30$ mTorr and $n_e = 5 \times 10^{19}$ m^{-3}, only ~14% of ionizations occur directly out of the ground state.

V. RESULTS AND DISCUSSION

The plasma density was measured with a cylindrical Langmuir probe that entered the RF discharge tube from the main chamber and could move along the tube axis (see Fig. 3). The probe tip surface area was $A = 4.5 \times 10^{-6}$ m^2, and the probe tip was located 1.4 cm inside the antenna for all measurements presented here. The ion saturation current ($I_{sat.}$) was measured, and the density was calculated using the results of numerical ion orbit calculations by Laframboise,[25] which gave the dimensionless parameter i_{+-} in the formula

$$n_e \approx n_i = \frac{I_{sat.}\sqrt{2\pi}}{eAc_s i_{+-}}, \qquad (10)$$

where $c_s = \sqrt{kT_e/m_i}$ is the ion acoustic velocity. T_e could not be measured accurately because the probe did not have RF compensation and the plasma inside the quartz discharge tube was not in good contact with a reference electrode, so the T_e value predicted by the global discharge model was used to evaluate c_s.

A. Time-dependent discharge behavior

The time-dependent discharge behavior is illustrated in Fig. 10. The RF amplifier was turned on and the UV flashlamp was pulsed to produce seed ionization at $t = 0$ μs. Initially, the source and load were mismatched, and the net power delivered to the load was well below 3 kW. At $t \sim 10$ μs, the plasma density had risen sufficiently to load the antenna and improve the impedance match, and P_L increased, allowing the discharge to transition to a much higher density mode of operation. The subsequent rapid density increase lagged the power rise by ~3 μs. The duration of the initial low-density phase could be altered by adjusting the matching capacitance C_s to vary the unloaded antenna voltage.

The power output of the RF amplifier gradually decreased in time as the 47 μF output stage capacitor discharged, with a proportional decline in the measured $I_{sat.}$. Since the time scale for these changes was much longer than the time scale for particle and energy losses from the discharge (a few μs), the discharge may be considered to have been in a quasi-steady state from $t = 30$–400 μs, with particle and energy balance satisfied, so the model of Sec. IV is applicable.

B. Plasma parameters achieved and evidence for inductively coupled operation

The measured scaling of ion saturation current with RF power and magnetic field is shown in Figs. 11 and 12. Data were taken at both 10 and 30 mTorr in the magnetized cases, while with $B = 0$, the discharge could only be initiated at $p_{Ar} \gtrsim 20$ mTorr. In Fig. 11(a), the data are compared with model predictions for $I_{sat.}$ (derived from Fig. 9(b) and similar results using Eq. (10)) for discharges with low voltage (ICP)

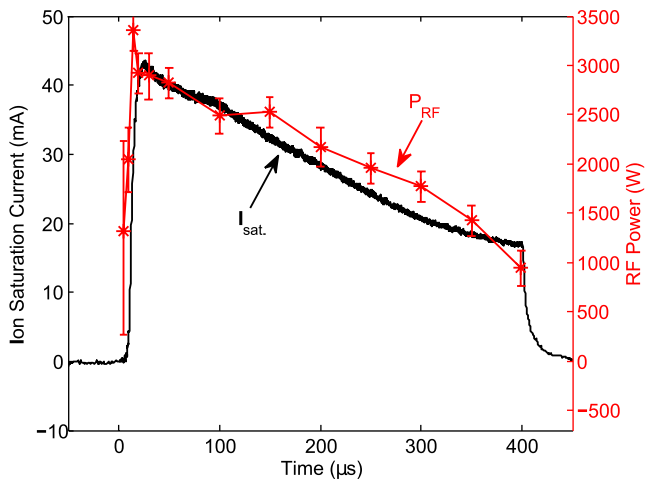

FIG. 10. Time-dependent ion saturation current (roughly proportional to n_e) and net RF power delivered to the load for a set of discharges with $B = 340$ G, $p_{Ar} = 30$ mTorr, and an RF pulse length of 400 μs.

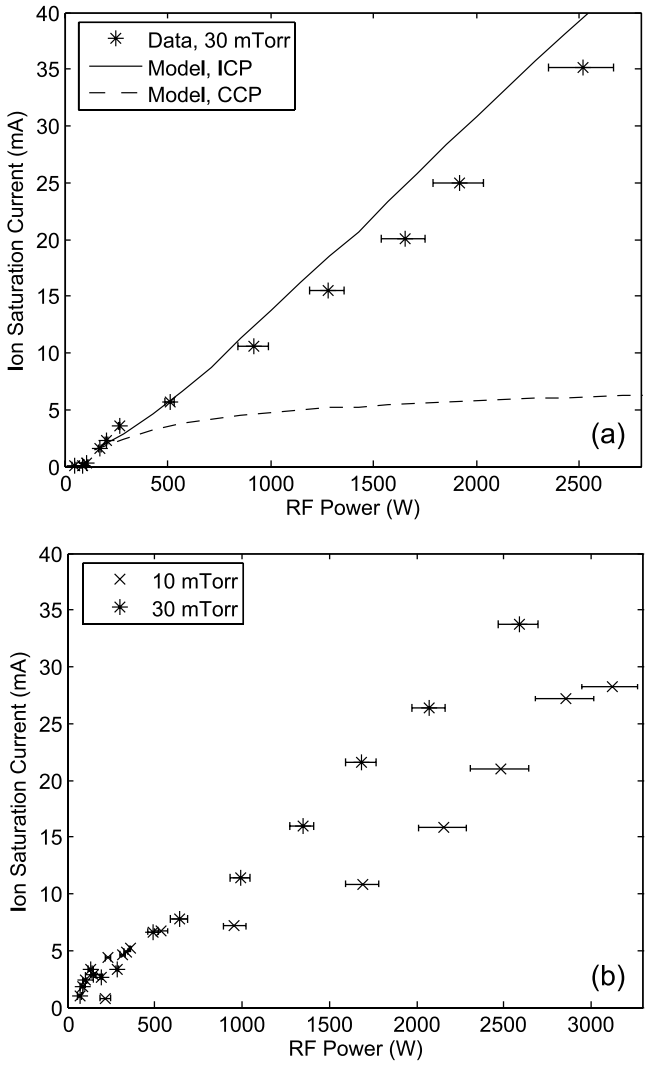

FIG. 11. Langmuir probe ion saturation current vs. RF power with $B = 0$ G (a) and $B = 340$ G (b). In panel (a), the solid and dotted lines show the model predictions for inductively coupled and capacitively coupled discharges, respectively, at 30 mTorr, assuming that 70% of the RF power delivered to the load was absorbed by the plasma.

and high voltage (CCP) sheaths. For the capacitively coupled calculation, $V_s = 0.4V_{antenna}$ was assumed. We only measured the net RF power delivered to the load as a whole; the fraction of this power that was actually absorbed by the plasma (rather than dissipated in the impedance matching capacitors and antenna resistance) is not known, but adopting a plausible value of 70% for the model calculation gives reasonably good agreement between the data and the ICP model. The $I_{sat.}$ values predicted by the CCP model, on the other hand, are far too low, indicating that the discharge could not have been primarily capacitively coupled.

When an axial magnetic field was applied, operation in an efficient helicon wave-heated mode was expected to be possible. The helicon dispersion relation[26] valid for the $m = 0$ and $m = 1$ azimuthal wave modes propagating in a long, thin discharge tube ($k_z \ll k$) is

$$\frac{\omega}{k_z} \approx \frac{B_0 Z_1}{\mu_0 e n_e R}, \tag{11}$$

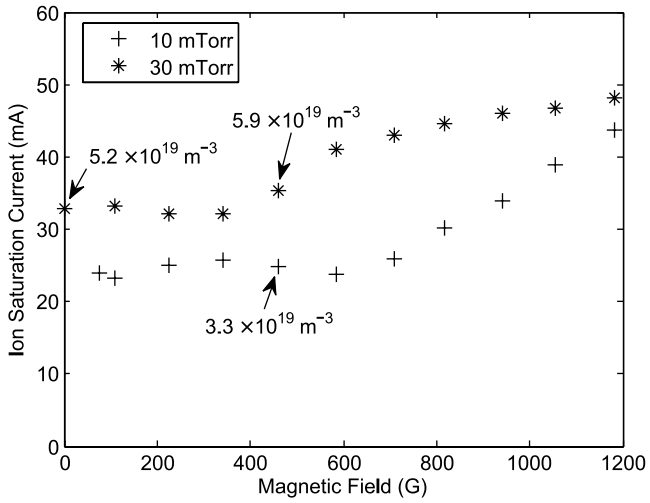

FIG. 12. Ion saturation current vs. axial magnetic field strength with $P_{RF} = 3.08 \pm 0.26$ kW. The $I_{sat.}$ values may be converted to plasma densities by using Eq. (10) and plugging in the electron temperatures predicted by the model for ICP discharges. For example, assuming that 70% of the RF power delivered to the load was absorbed by the plasma; at $p_{Ar} = 30$ mTorr and $B = 0$ G, the model gives $T_e = 2.25$ eV; then from Eq. (10), $I_{sat.} = 32.9$ mA corresponds to $n_e = 5.2 \times 10^{19}$ m^{-3}. A similar calculation for the data taken with $B = 470$ G gives $n_e = 3.3 \times 10^{19}$ m^{-3} at 10 mTorr and $n_e = 5.9 \times 10^{19}$ m^{-3} at 30 mTorr (where we assumed for a rough model calculation of T_e that magnetic confinement reduced the radial loss rate by a factor of 2).

where Z_1 is a zero of the Bessel function $J_1(x)$. Considering the axial currents it induces, the half-turn helical antenna used in our experiments is a half-wavelength structure,[27] so a reasonable assumption was that the helicon wavelength would be roughly $\lambda_z \approx 2L_{ant.}$.[26,28] Setting $Z_1 = 3.83$ for the first radial mode, Eq. (11) then gives $n_e = (6.1 \times 10^{20}) B_0$ in Systeme International (SI) units. Thus, with $B_0 = 100$ G, we anticipated that a plasma density $n_e \approx 6 \times 10^{18}$ m^{-3} would be required for efficient helicon propagation, while at $B_0 = 1000$ G, $n_e \approx 6 \times 10^{19}$ m^{-3} was expected to be required. This density range was readily accessible in our source (see Figs. 11(b) and 12), so helicon waves should have been excited. However, there were a number of pieces of indirect experimental evidence that damping of these waves or the related Trivelpiece-Gould mode[16,17] was not the primary mechanism for energy transfer to the plasma.

- The plasma densities obtained with and without a magnetic field were similar (compare the 30 mTorr data in Figs. 11(a) and 11(b)). Helicon sources can typically create plasma more efficiently than unmagnetized ICPs; this is thought to be because wave-particle interactions reduce the collisional energy loss per ionization event to near the ionization potential.[26,28] However, we did not see the expected degree of improvement when the magnetic field was turned on, which should have increased the density both by improving confinement and by allowing for helicon wave propagation.
- n_e was nearly constant as a function of B for $B \leq 500$ G and increased only gradually at higher fields (Fig. 12). In contrast, a rough scaling of density with field strength has been observed in many helicon

experiments[28,29] due to the linear proportionality between n_e and B_0 in Eq. (11), with transitions between different axial or radial modes leading to jumps in the n_e vs. B relation.

- As the RF power was increased in Fig. 11(b), no density jump indicating a transition from a CCP or an ICP mode to the helicon mode was seen, unlike in other helicon sources.[27,30]
- The effectiveness of the half-turn helical antenna at producing plasma was unchanged when the direction of the magnetic field was reversed, in contrast to the behavior of other experiments in which helicon mode operation has been demonstrated.[14,15]

Based on these observations, we may conclude that inductive coupling rather than wave heating was the dominant energy transfer mechanism in our RF plasma source. To confirm that the short RF pulse length was not to blame for the lack of helicon mode operation, we tried increasing the RF amplifier's output stage capacitance from 47 μF to 188 μF, enabling >2 ms RF pulses. The observed density scaling behaviors were unchanged.

The narrow 1.1 cm discharge tube radius is another factor that could inhibit helicon mode operation due to electrostatic charging of the tube walls or other boundary effects.[31] Although a number of other authors have labeled their small radius ($R < 2$ cm) RF discharges as helicon sources,[10,11,32–34] the presence of propagating waves was not directly verified in any of these experiments. Only Shinohara *et al.*[33] found compelling evidence for helicon mode operation by identifying two separate mode transitions from a CCP mode to an ICP mode and then to a helicon mode. Given that there are a number of practical uses for small RF plasma sources,[11,32,34] we expect that additional dedicated experiments designed to explore the scaling of helicon source operation with tube radius would yield interesting, useful results.

The $\sim 5 \times 10^{19}$ m^{-3} peak density achieved in our source with $B = 0$ places it in a rather unique regime; we know of only one other experiment[32] in which $n_e > 10^{19}$ m^{-3} has been achieved in a low pressure RF plasma source operating in an unmagnetized ICP mode. Low pressure ICPs excited by multi-turn coils are typically limited to operating at $n_e \leq 10^{19}$ m^{-3} because the large coil currents needed to achieve higher densities lead to excessive resistive dissipation in the coil.[35] However, no density limit was evident as P_{RF} was increased in our source (see Fig. 11(a)). Further work is needed to determine whether the observed density scaling is unique to the half-turn helical antenna, or if it is a general property of small-volume discharges with high power input density.

C. Formation of MHD-driven jets aided by pre-ionization

As anticipated, the installation of the RF pre-ionization source on the MHD-driven jet experiment allowed for plasma breakdown at lower neutral gas pressures than had been previously possible. For jet experiments, there was no uniform argon backfill; instead, three fast pulsed gas valves[18] were used to inject gas through small holes in the jet experiment's cathode and anode (see Figs. 1 and 3), and also into the RF plasma source tube. The gas injection was timed so that gas was present only in the immediate vicinity of the electrodes, allowing the jet to propagate into vacuum after its formation.

The quantity of gas injected was controlled by varying the charging voltage of the capacitor banks powering the fast gas valves; the flow rate of gas exiting each valve was an increasing, nonlinear function of the bank voltage.[18] The gas density distribution at the time when the electrodes were energized was not measured in this work, but it was possible to make inferences about the relative gas pressures in different situations based on the known properties of the gas valves[36] and on the observed jet velocity.

With the RF source gas bank voltage set to $V_{gas,RF}$ = 550 V, it was possible to get full plasma breakdown and

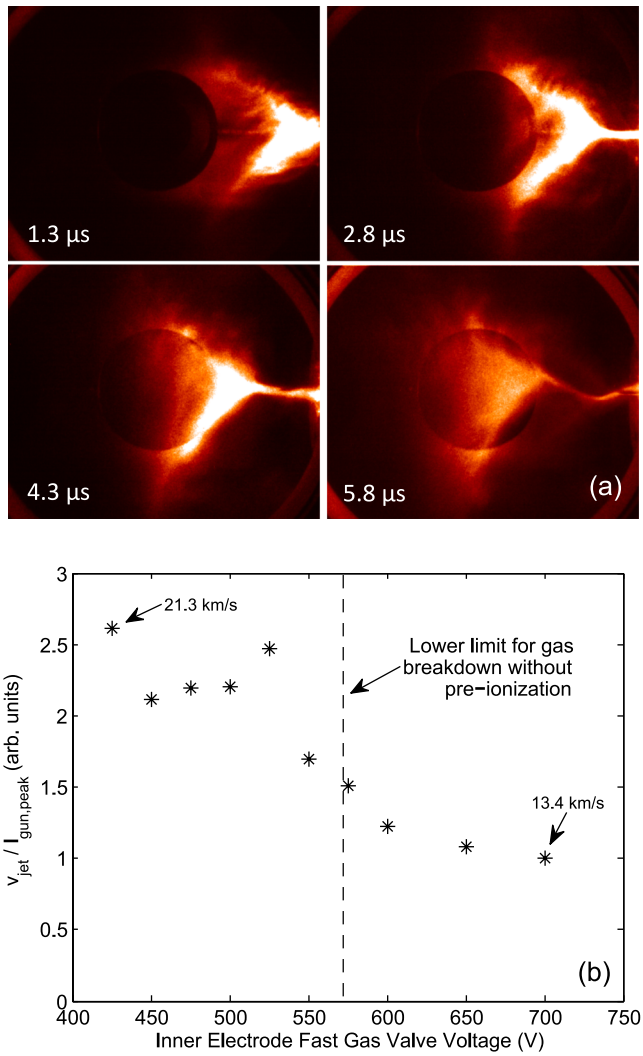

FIG. 13. (a) False-colored images of a pre-ionized jet created with $V_{gas,inner}$ = 460 V and $V_{gas,outer}$ = 709 V, taken with an Imacon 200 high speed movie camera. The electrodes and pre-ionization source are beyond the right edge of the images, and the jet is propagating to the left (the orientation is the opposite of that in Fig. 3). The circular object in the center of the images is a window on the far side of the vacuum chamber; the portions of the jet that are not in front of the window appear brighter because the chamber walls are highly reflective. (b) Argon jet velocities measured from fast camera images with $V_{gas,outer}$ = 709 V and variable $V_{gas,inner}$, normalized to the peak main bank current for each shot. The main bank charging voltage was −4 kV.

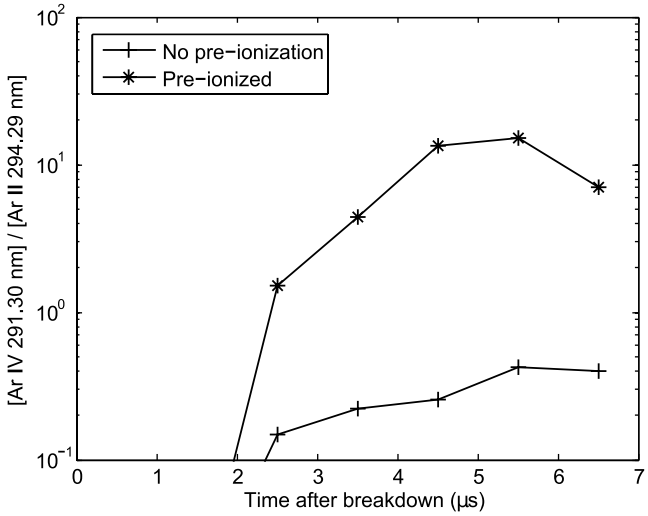

FIG. 14. [Ar IV 291.30 nm]/[Ar II 294.29 nm] emission line intensity ratio measured with a 1 m Czerny-Turner spectrometer with a gated ICCD detector. The shots labeled "no pre-ionization" had $V_{gas,inner} = 700$ V and $V_{gas,outer} = 750$ V, while the pre-ionized shots used $V_{gas,inner} = 0$ V, $V_{gas,outer} = 750$ V, and $V_{gas,RF} = 525$ V. The main bank charging voltage was −4 kV for all shots.

initiate the main arc discharge even if no gas was injected through the inner and outer electrodes—we estimate that the total mass of gas in the chamber in this case was at least four times less than was needed to achieve breakdown in the absence of pre-ionization. However, a well-defined jet would not form unless a substantial quantity of gas was puffed in through the outer electrode, probably because there was no pre-ionized plasma present in the vicinity of the outer electrode.

While holding the outer electrode gas bank voltage constant at $V_{gas,outer} = 709$ V, the inner electrode gas bank voltage was varied, and the jet velocity was measured by identifying the jet front location in fast movie camera images. Examples of such images are shown in Fig. 13(a), and the velocities obtained are shown in Fig. 13(b). When the pre-ionization source was not used, plasma breakdown could not be achieved with $V_{gas,inner} \leq 570$ V. Pre-ionization enabled us to access the new regime to the left of the dotted line in Fig. 13(b).

Previous experiments and theoretical work[7] have demonstrated that the jet velocity scales as $v_{jet} \sim I/\sqrt{\rho_0 a^2} \sim I/\sqrt{N/L}$, where I is the axial (poloidal) current driving the jet, ρ_0 is the mass density on axis, a is the jet radius, and N/L is the number of particles per unit length. The velocities in Fig. 13(b) were normalized to the peak I for each shot in order to derive a quantity that scales as $(N/L)^{-1/2}$. Neglecting small differences in the lengths of the jets, we may infer that pre-ionization allowed the jet mass to be decreased by a factor of $\sim(2.6/1.5)^2 \approx 3$. The lower mass jets were expected to be hotter than those created without pre-ionization, and indeed, spectroscopic measurements (Fig. 14) showed more than an order of magnitude increase in the ratio of Ar IV to Ar II emission, indicating a higher mean ionization state of the plasma.

In jet experiments with a low level of gas input, pre-ionization dramatically reduced the delay and shot-to-shot variation in the breakdown time. For example, in a set of experiments with $V_{gas,outer} = 709$ V and $V_{gas,inner} = 575$ V, breakdown occurred anywhere from 7.7 to 15.4 μs after the electrodes were energized when no pre-ionization was used, while with pre-ionization, the range in breakdown times was 1.9–2.3 μs.

VI. CONCLUSION

We have described the design and characterization of a pre-ionization plasma source powered by an electrically floating pulsed 13.56 MHz RF power amplifier. Plasma densities exceeding 5×10^{19} m^{-3} were achieved in inductively coupled operation with and without a background magnetic field. The installation of the pre-ionization source on the Caltech MHD-driven jet experiment enabled the creation of argon plasma jets that were lighter, hotter, and faster than was possible without pre-ionization. Our RF plasma source should be widely applicable to other experiments in which the requirements for Paschen breakdown are incompatible with the desired plasma parameters. The RF amplifier can also be used as a stand-alone power source; the combined weight of the amplifier, matching network, and batteries is ∼1 kg, making it well suited for a variety of portable applications. With cooling added as described in Ref. 20, the amplifier could be operated as a CW 3 kW RF source, or it may be easily modified to operate at much lower power. This has been done for a small dusty plasma experiment at Caltech[37] that operates with 1–3 W of power capacitively coupled to the plasma.

ACKNOWLEDGMENTS

This material is based upon work supported by the U.S. Department of Energy Office of Science, Office of Fusion Energy Sciences under Award Nos. DE-FG02-04ER54755 and DE-SC0010471 and by the National Science Foundation under Award No. 1059519. V. H. Chaplin acknowledges support by the ORISE Fusion Energy Sciences Graduate Fellowship.

[1]S. C. Hsu and P. M. Bellan, Phys. Plasmas **12**, 032103 (2005).
[2]E. V. Stenson and P. M. Bellan, Phys. Rev. Lett. **109**, 075001 (2012).
[3]D. Kumar, A. L. Moser, and P. M. Bellan, IEEE Trans. Plasma Sci. **2**, 47 (2010).
[4]M. J. Aschwanden, *Physics of the Solar Corona: An Introduction with Problems and Solutions*, 2nd ed. (Springer, New York, 2005).
[5]M. D. Smith, *Astrophysical Jets and Beams* (Cambridge University Press, Cambridge, 2012).
[6]S. C. Hsu and P. M. Bellan, Phys. Rev. Lett. **90**, 215002 (2003).
[7]D. Kumar and P. M. Bellan, Phys. Rev. Lett. **103**, 105003 (2009).
[8]A. L. Moser and P. M. Bellan, Nature **482**, 379 (2012).
[9]M. A. Lieberman and A. J. Lichtenberg, *Principles of Plasma Discharges and Materials Processing*, 2nd ed. (Wiley-Interscience, Hoboken, N.J., 2005).
[10]K. Toki, S. Shinohara, T. Tanikawa, and K. P. Shamrai, Thin Solid Films **506–507**, 597 (2006).
[11]P. Kerdtongmee, D. Srinoum, and M. Nisoa, Rev. Sci. Instrum. **82**, 103503 (2011).
[12]A. C. Hossack, T. Firman, T. R. Jarboe, J. R. Prager, B. S. Victor, J. S. Wrobel, and T. Ziemba, Rev. Sci. Instrum. **84**, 103506 (2013).
[13]P. K. Chattopadhyay, R. Pal, N. R. Ray, and P. K. Gupta, Nucl. Fusion **36**, 1205 (1996).
[14]T. Shoji, Y. Sakawa, S. Nakazawa, K. Kadota, and T. Sato, Plasma Sources Sci. Technol. **2**, 5 (1993).

[15]F. F. Chen, I. D. Sudit, and M. Light, Plasma Sources Sci. Technol. **5**, 173 (1996).
[16]K. P. Shamrai and V. B. Taranov, Plasma Sources Sci. Technol. **5**, 474 (1996).
[17]F. F. Chen and D. D. Blackwell, Phys. Rev. Lett. **82**, 2677 (1999).
[18]P. M. Bellan, Rev. Sci. Instrum. **73**, 2900 (2002).
[19]*DRF1301 MOSFET Push-Pull Hybrid*, Microsemi, 2011.
[20]G. Choi, 13.56 MHz, Class D Push-Pull, 2KW RF Generator with Microsemi DRF1300 Power MOSFET Hybrid, Microsemi, 2011, application note 1812.
[21]R. W. Boswell and D. Vender, Plasma Sources Sci. Technol. **4**, 534 (1995).
[22]S. Ashida, C. Lee, and M. A. Lieberman, J. Vac. Sci. Technol., A **13**, 2498 (1995).
[23]M.-H. Lee and C.-W. Chung, Appl. Phys. Lett. **87**, 131502 (2005).
[24]G. B. Rybicki and A. P. Lightman, *Radiative Processes in Astrophysics*, 2nd ed. (Wiley-VCH, Germany, 2004).
[25]J. G. Laframboise, "Theory of spherical and cylindrical Langmuir probes in a collisionless, Maxwellian plasma at rest," Technical Report 100, Institute for Aerospace Studies, University of Toronto, 1966.
[26]F. F. Chen, Plasma Phys. Controlled Fusion **33**, 339 (1991).
[27]A. R. Ellingboe and R. W. Boswell, Phys. Plasmas **3**, 2797 (1996).
[28]R. W. Boswell, Plasma Phys. Controlled Fusion **26**, 1147 (1984).
[29]F. F. Chen and R. W. Boswell, IEEE Trans. Plasma Sci. **25**, 1245 (1997).
[30]C. M. Franck, O. Grulke, and T. Klinger, Phys. Plasmas **10**, 323 (2003).
[31]F. F. Chen, J. Vac. Sci. Technol., A **10**, 1389 (1992).
[32]D. Kuwahara, A. Mishio, T. Nakagawa, and S. Shinohara, Rev. Sci. Instrum. **84**, 103502 (2013).
[33]S. Shinohara, T. Hada, T. Motomura, K. Tanaka, T. Tanikawa, K. Toki, Y. Tanaka, and K. P. Shamrai, Phys. Plasmas **16**, 057104 (2009).
[34]O. V. Batishchev, IEEE Trans. Plasma Sci. **37**, 1563 (2009).
[35]M. A. Lieberman and A. J. Lichtenberg, *Principles of Plasma Discharges and Materials Processing*, 2nd ed. (Wiley-Interscience, Hoboken, N.J., 2005), section 12.1.
[36]V. H. Chaplin, "Battery-powered RF pre-ionization system for the Caltech magnetohydrodynamically-driven jet experiment: RF discharge properties and MHD-driven jet dynamics," Ph.D. thesis, California Institute of Technology, 2015.
[37]K. B. Chai and P. M. Bellan, Geophys. Res. Lett. **40**, 6258, doi:10.1002/2013GL058268 (2013).